Computational Mechanics of the Heart

From Tissue Structure to Ventricular Function

M. P. NASH
University Laboratory of Physiology, University of Oxford, Parks Road, Oxford OX1 3PT, U.K.
E-mail: martyn.nash@physiol.ox.ac.uk

P. J. HUNTER
Department of Engineering Science, The University of Auckland, Auckland, New Zealand.
E-mail: p.hunter@auckland.ac.nz

Abstract. Finite elasticity theory combined with finite element analysis provides the framework for analysing ventricular mechanics during the filling phase of the cardiac cycle, when cardiac cells are not actively contracting. The orthotropic properties of the passive tissue are described here by a "pole–zero" constitutive law, whose parameters are derived in part from a model of the underlying distributions of collagen fibres. These distributions are based on our observations of the fibrous-sheet laminar architecture of myocardial tissue. We illustrate the use of high order (cubic Hermite) basis functions in solving the Galerkin finite element stress equilibrium equations based on this orthotropic constitutive law and for incorporating the observed regional distributions of fibre and sheet orientations. Pressure–volume relations and 3D principal strains predicted by the model are compared with experimental observations. A model of active tissue properties, based on isolated muscle experiments, is also introduced in order to predict transmural distributions of 3D principal strains at the end of the contraction phase of the cardiac cycle. We end by offering a critique of the current model of ventricular mechanics and propose new challenges for future modellers.

1. Introduction

The heart is an electro-mechanical pump with remarkable properties, but one whose failure is the leading non-accidental cause of death in developed countries. The mechanical function of the heart depends crucially on its material properties. Understanding these properties in relation to the structure of the tissue, and how changes in the tissue structure thereby affect the pumping function of the intact heart, is a central goal of cardiac mechanics research. The purpose of this paper is to review our current knowledge of myocardial structure and the models used to describe it, and to show how the material constitutive laws are used to understand the mechanics of the heart via finite element analysis of the right and left ventricles.

Analyzing the behaviour of any soft biological tissue, at the isolated tissue level and the intact organ level, presents many fascinating challenges to both the experimental materials scientist and the computational modeller. Soft tissues are invariably anisotropic and inhomogeneous, exhibit nonlinear and time-dependent properties, and can seldom be treated within just a mechanics framework since they are often electrically active, contain blood vessels and grow! The complex anatomy of a soft tissue organ also presents a computational challenge, because there are no axes of symmetry to exploit and boundary loads are invariably spatially nonuniform and time-varying. Of course, this complexity is precisely what makes the study of soft tissue so interesting. Fortunately, we have sufficient computational resource to solve the relevant boundary value problems and sufficient graphics capability on a desktop computer to display the results of 3D computational modelling.

One of the most comprehesive reviews of early cardiac mechanics modelling is provided by [45], which summarises the evolution from the late nineteenth century thin-walled analytical models of ventricular wall stress [43] to the biophysically realistic computational models during the 1970's. Key developments during this period include:

  (i) the necessity to incorporate finite deformation analysis as opposed to the small-strain (a.k.a. classical or linear) elasticity theory (first illustrated by [26]);

 (ii) the use of the finite element method (FEM) to efficiently and accurately describe the complex geometry of the ventricles (one of the earliest finite element (FE) models of left ventricle (LV) mechanics was formulated by [9]);

(iii) the significance of material anisotropy and heterogeneity on predicted wall stress [15]; and

(iv) the use of nonlinear stress-strain relations to predict more realistic wall deformations [16].

Subsequent reviews of [12, 24] describe how recent models of cardiac mechanics have integrated the developments of the earlier studies with detailed experimental measurements of anatomical geometry, tissue microstructure and myocardial material properties for both resting and active tissue.

The plan for this review of cardiac mechanics modelling is as follows. We first describe the biological structure – the anatomy of the heart and its microstructural architecture. We then present a mathematical framework for describing the finite elastic deformation of inhomogeneous, incompressible, anisotropic soft tissue, and how cubic Hermite finite element basis functions can be used to approximate the geometric fields describing the deformations that occur as the heart beats. A Galerkin finite element approximation of the stress equilibrium equations is presented and appropriate constitutive laws are formulated together with their underlying microstructural basis. Finally, a finite element model of the left and right ventricular myocardium, with a fibrous-sheet structure fitted from canine heart measurements, is loaded as it would be during the filling phase of the cardiac

cycle and at the end of the contraction phase to demonstrate the importance of the anisotropic and inhomogeneous material properties described earlier.

2. The Anatomy and Tissue Structure of the Heart

The primary function of the heart is to pump blood throughout the body, delivering nutrients and removing wastes from each organ. The heart has four chambers: the *left* and *right ventricles* and the *left* and *right atria* (refer to Figure 1). The thinner-walled atria act as large low pressure blood reservoirs for the ventricles which are the predominant pumping chambers. Atrial myocardium is separated from that of the ventricles by the *basal skeleton*, which is a fibrous framework formed by the rings of four valves and surrounding connective tissue. The two *atrioventricular valves* connect the atria to their respective ventricles. The *mitral valve* consists of two leaflets (bicuspid) and prevents back flow from the LV to the left atrium (LA). Similarly the *tricuspid valve* controls the passage of blood from the right atrium (RA) to the right ventricle (RV). The remaining two *semilunar valves* join the outflow tracts of each ventricle with the great arteries into which the ventricle ejects blood. The *pulmonary valve* ensures forward flow of blood from the RV into the *pulmonary artery* and the *aortic valve* ensures blood flow from the LV into the *aorta*.

   The LV is a thick-walled muscular chamber that pumps blood at physiologically high pressures (up to approximately 15 kPa or 110 mmHg during the normal heart cycle) to distal locations throughout the body. The cavity of the LV resembles a truncated ellipsoid in which both the inflow and outflow tracts are adjacent. In contrast, the RV pumps blood at comparatively low pressures (about one seventh the pressure of the LV) and wraps around the LV in a crescent-like fashion so that
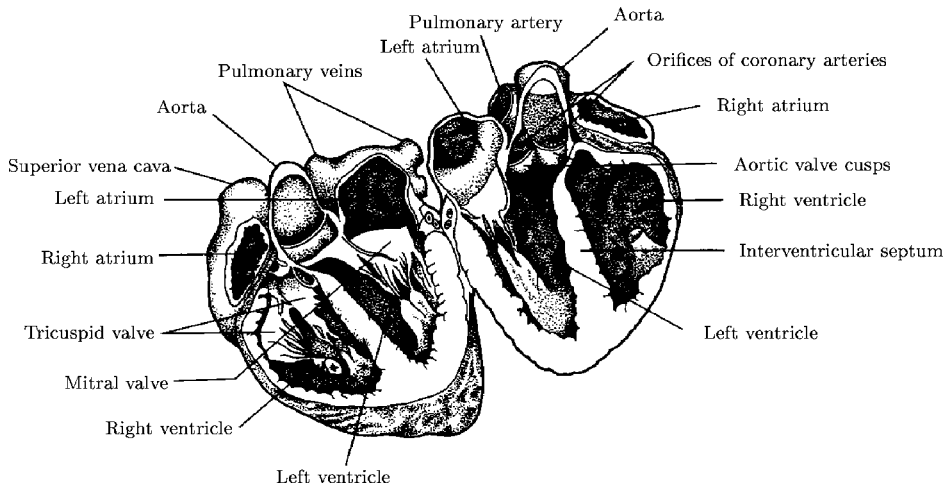

Figure 1. Longitudinal cross-section of the heart. From [18].

its cavity forms a shallow U-shape. The ventricles are separated by the *interventricular septum*, which normally functions as part of the LV and moves toward the LV free wall during *systole* (the contraction phase of the cardiac cycle).

Cardiac muscle cells or *myocytes* are typically cylindrical with lengths that range from 80 to 100 μm and diameters ranging from 10 to 20 μm. The fundamental contractile unit is the *sarcomere*, which is about 2 μm in length. The sarcomere spans between adjacent *Z-lines* along the longitudinal axis of the cell and contains the contractile apparatus. Cells consist of about 40–50 sarcomeres in series and branch and interconnect end-to-end through *intercalated disk junctions*. The branching angle is usually acute so that adjacent cells run almost parallel to one another. In this way, the contractile apparatus between cells is aligned for efficient mechanical function. Intercalated disks contain *nexi* or *gap junctions*, which provide electrical continuity between cells. Consequently, the electrical impulses propagate more rapidly along rather than across the axes of the muscle fibres.

Muscle cells within the cardiac walls generate contractile forces upon electrical depolarisation. Each cell is excited in turn as a wave of electrical activation propagates throughout the myocardium. Activation normally begins spontaneously in pacemaker cells of the *sinoatrial node*, which lies between the superior vena cava and the right atrium (see Figure 1). The first structures to be depolarised during the normal cardiac cycle are the atria. As the wave of electrical activation propagates throughout the atria, they contract and pump blood into their respective ventricles, which marks the final stage of ventricular filling. The ventricular myocardium is normally electrically isolated from the atria except for a group of slow conducting cells known as the *atrioventricular (AV) node*. This provides enough time for the atrial blood to be pumped into the ventricles prior to ventricular contraction.

The activation wave reaches the ventricular myocardium via the *AV bundle* (also known as the *common bundle*, or *bundle of His*), which bifurcates into *right* and *left bundle branches* at the top of the interventricular septum. Each branch passes down the septum and curls around into the apical portions of its respective ventricle. At this point the bundles divide into networks of fast conducting *Purkinje fibres*, which spread over and deliver the electrical impulse to the inner or *endocardial* portions of the ventricular myocardium. The activation wave generally proceeds from endocardial layers to the *epicardial* or outer portions of the ventricular myocardium. As the wave of excitation propagates, individual myocardial cells are sequentially stimulated to generate tensile forces and contract. At a macroscopic level, this causes the ventricles to contract and pump blood to the body.

Electrical activation initiates cell contraction, but also mechanical contraction affects the propagating electrical wave – especially during the reentrant arrhythmias that precede ventricular fibrillation. Changes in cell length and the cross-sectional area of cells have a direct effect on propagation pathways and also change the conductance of ion channels, thereby altering membrane potential. Some ion channels are in fact activated by supra-threshold levels of stretch (so-called *stretch activated channels* or SACs) [18].
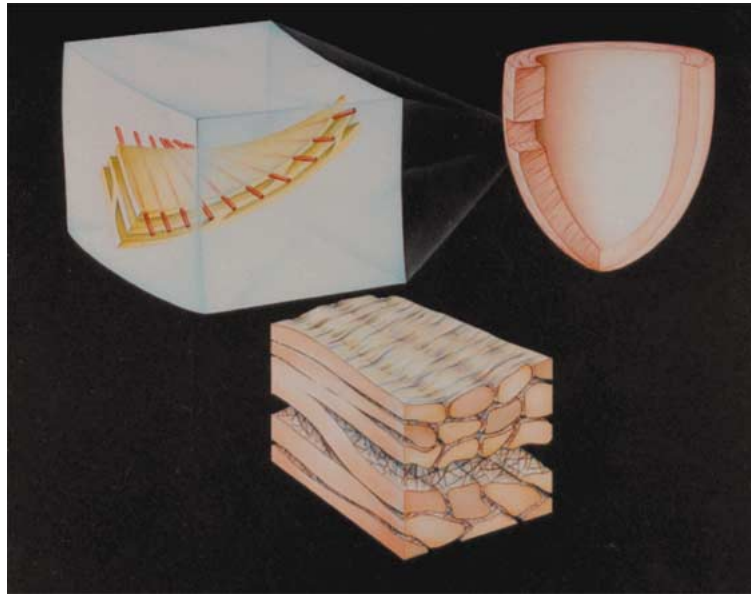
Figure 2. Schematic of cardiac microstructure showing fibre orientation and branching sheet structures. A transmural block of tissue (top left) from the wall of the LV (top right) contains *myocardial sheets* (yellow) comprised of myocytes, whose axes (red) define the *fibre direction*. These sheets interconnect (bottom) and are bound together by endomysial collagen surrounding the sheets and perimysial collagen between the sheets. From [19] by permission of the *American Journal of Physiology*.

Recent anatomical studies [19, 28] have shown that cardiac tissue is a composite of discrete layers of myocardial muscle fibres tightly bound by *endomysial collagen*, as illustrated in Figure 2. These *myocardial laminae* or *sheets* are loosely coupled by *perimysial collagen* and have the ability to slide over each other with relative ease [20]. Laminae are on average four to six cells thick and continuously branch in each direction throughout the ventricular walls. Their orientation is generally normal to the ventricular surfaces, except in the subendocardial and subepicardial regions, where they appear to become more aligned with the wall surfaces.

The *pericardium* is a fibrous sac that encompasses the entire heart to resist rapid increases in cardiac size. The inner wall of this sac is called the *parietal pericardium* and is continuous with the *epicardium* or *visceral pericardium* (the layer of connective tissue on the outer ventricular surface) at the base of the heart, where the great vessels enter and leave. A small amount of fluid within the pericardial sac provides lubrication for the continuous movement of the heart. The pericardium affects myocardial deformation and will need to be considered in future models of ventricular mechanics (see later).

The heart is nourished by blood flow through a network of vessels known as the *coronary vascular system*. These blood vessels enter the ventricular wall

from the outside and bifurcate through about seven generations of *arteries* and *arterioles* before merging into a *capillary cascade*, where gas exchange with the tissue takes place. At this level, a cross-section of the muscle reveals a one-to-one ratio of capillaries to myocytes. The capillaries collect into *venules* and then *veins*, which eventually empty the de-oxygenated blood into the RA. Coronary flow is strongly influenced by myocardial mechanics. During systolic contraction, for example, arterial flow in the subendocardium is briefly reversed as the ventricles are compressed by the surrounding active muscle. Similarly, the mechanical deformation of the myocardial tissue is influenced by coronary perfusion in at least two respects: the spatially and temporally changing coronary blood pressure influences the tissue hydrostatic pressure; and the shift of fluid volume, especially during systole, introduces an effective compressibility into the otherwise incompressible tissue.

3. The Theory of Finite Elastic Deformations

Cardiac cells change length by over 20% during a normal heart beat, so mechanical analysis must be based on finite deformation elasticity theory. We first describe the kinematics of large deformation, then stress equilibrium and the finite element basis functions that extend the analysis to complex 3D ventricular shapes.

3.1. KINEMATICS

$\mathbf{x} = (x_1, x_2, x_3)$ gives the present position in rectangular cartesian coordinates of a material particle that occupied the place $\mathbf{X} = (X_1, X_2, X_3)$ in the reference state. In standard finite deformation theory, (X_1, X_2, X_3) are considered as material coordinates and a *deformation gradient tensor* $\mathbf{F}$ is defined, which carries the line segment $d\mathbf{X}$ into $d\mathbf{x} = \mathbf{F} \, d\mathbf{X}$, or in component form, $dx^i = F^i_M \, dX^M$, where

$$F^i_M = \frac{\partial x_i}{\partial X_M}. \tag{1}$$

Polar decomposition, $\mathbf{F} = \mathbf{RU}$, splits $\mathbf{F}$ into the product of an orthogonal rotation tensor $\mathbf{R}$ and a symmetric positive definite stretch tensor $\mathbf{U}$ which contains a complete description of the material strain, independent of any rigid body motion (see [1]).

For inhomogeneous, anisotropic materials the orientation of the material axes may vary with location and so it is no longer convenient to identify the material axes in the undeformed body with the reference coordinates. Instead, a new material coordinate system (ν_1, ν_2, ν_3) is introduced, which is aligned with certain structural features of the material. For myocardium, a natural set of material axes are formed by identifying ν_1 with the muscle fibre direction, ν_2 with the sheet direction and ν_3 with the sheet-normal direction (refer to Figure 3). It is convenient to choose the base vectors for the ν_α-coordinate system to be orthogonal in the reference state. However, the ensuing deformation means that they are not orthogonal, in general, in the deformed configuration.
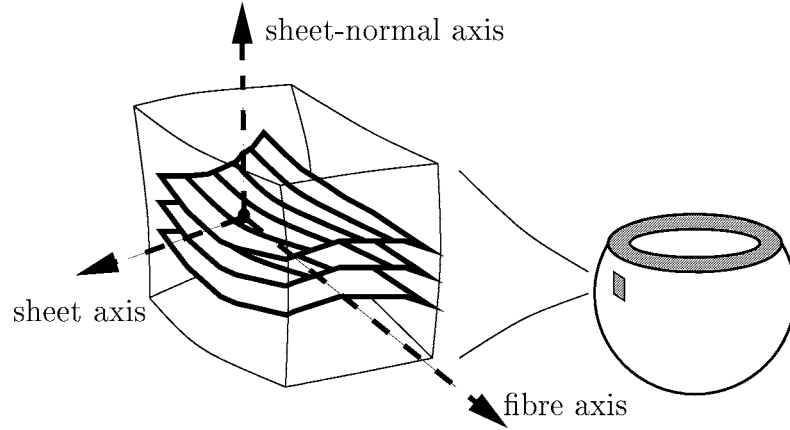
Figure 3. Microstructural material axes for myocardial tissue. The first of these directions is referred to as the *fibre axis* and coincides with the muscle fibre direction at each point. The *sheet axis* is defined to lie in the plane of the muscle layer and is perpendicular to the fibre direction. The third axis is defined to be orthogonal to the first two and is referred to as the *sheet-normal axis* as it is perpendicular to the muscle layer.

$\mathbf{A}_\alpha^{(\nu)}$, $\mathbf{A}_{(\nu)}^\alpha$ and $\mathbf{a}_\alpha^{(\nu)}$, $\mathbf{a}_{(\nu)}^\alpha$ denote the covariant and contravariant base vectors in the undeformed (upper-case) and deformed (lower-case) configurations, respectively. The corresponding metric tensors are denoted by $A_{\alpha\beta}^{(\nu)}$, $A_{(\nu)}^{\alpha\beta}$ and $a_{\alpha\beta}^{(\nu)}$, $a_{(\nu)}^{\alpha\beta}$. The undeformed covariant base vectors $\mathbf{A}_\alpha^{(\nu)}$ can be defined to be unit vectors by choosing the ν_α-coordinates to be a measure of physical arc-length in the undeformed state. The covariant base vectors and metric tensors for the ν_α-coordinate system are:

$$
\begin{aligned}
\mathbf{A}_\alpha^{(\nu)} &= \frac{\partial X_k}{\partial \nu_\alpha} \mathbf{g}_k^{(x)}, & \mathbf{a}_\alpha^{(\nu)} &= \frac{\partial x_k}{\partial \nu_\alpha} \mathbf{g}_k^{(x)}, \\
A_{\alpha\beta}^{(\nu)} &= \mathbf{A}_\alpha^{(\nu)} \cdot \mathbf{A}_\beta^{(\nu)}, & a_{\alpha\beta}^{(\nu)} &= \mathbf{a}_\alpha^{(\nu)} \cdot \mathbf{a}_\beta^{(\nu)},
\end{aligned}
\tag{2}
$$

where $\mathbf{g}_k^{(x)}$ are the base vectors of the rectangular Cartesian reference axes.

The Green strain tensor with respect to fibre-sheet material coordinates is then

$$
E_{\alpha\beta} = \frac{1}{2}\big(a_{\alpha\beta}^{(\nu)} - A_{\alpha\beta}^{(\nu)}\big).
\tag{3}
$$

3.2. STRESS EQUILIBRIUM AND THE PRINCIPLE OF VIRTUAL WORK

Stress equilibrium is expressed via the following equation derived from the principle of virtual work:

$$
\begin{aligned}
&\int_{V_0} T^{\alpha\beta} F_\beta^j \delta v_{j,\alpha} \, \mathrm{d}V_0 \\
&= \int_{V_0} \rho_0\big(b^j - f^j\big)\delta v_j \, \mathrm{d}V_0 + \int_{S_2} p_{(\mathrm{appl})} \frac{g_{(\xi)}^{3M}}{\sqrt{g_{(\xi)}^{33}}} \frac{\partial x_j}{\partial \xi_M} \delta v_j \, \mathrm{d}S,
\end{aligned}
\tag{4}
$$

where $T^{\alpha\beta}$ and $F_\beta^j (= \partial x_j / \partial \nu_\beta)$ are respectively the second Piola–Kirchhoff stresses and deformation gradients expressed relative to the fibre-sheet material coordinates, $\delta\mathbf{v} = \delta v_j \mathbf{i}_j$ are virtual displacements expressed relative to the reference coordinate system (see [23]), ρ_0 is the tissue density, b^j and f^j are respectively the components of the body force and acceleration vectors, $p_{(\text{appl})}$ is the pressure (i.e., physical stress) applied to the surface S_2 with normal direction ξ_3, and $g_{(\xi)}^{MN}$ are contravariant metric tensors for the ξ_M coordinate system (described below), with covariant base vectors and metric tensors for the undeformed and deformed states defined by:

$$\mathbf{G}_M^{(\xi)} = \frac{\partial X_k}{\partial \xi_M} \mathbf{g}_k^{(x)}, \qquad\qquad \mathbf{g}_M^{(\xi)} = \frac{\partial x_k}{\partial \xi_M} \mathbf{g}_k^{(x)},$$
$$G_{MN}^{(\xi)} = \mathbf{G}_M^{(\xi)} \cdot \mathbf{G}_N^{(\xi)} = \frac{\partial X_k}{\partial \xi_M} \frac{\partial X_k}{\partial \xi_N}, \qquad g_{MN}^{(\xi)} = \mathbf{g}_M^{(\xi)} \cdot \mathbf{g}_N^{(\xi)} = \frac{\partial x_k}{\partial \xi_M} \frac{\partial x_k}{\partial \xi_N}. \tag{5}$$

Equation (4) is the starting point for the analysis of a body undergoing large elastic deformations. For further details see [3, 4].

3.3. RESIDUAL STRAIN

Mathematical models of large deformation mechanics compute material strains (and hence stresses) with respect to a well defined reference configuration, for which the strain components are usually assumed to be zero. However, if no such state exists for an intact specimen such as the heart, the closest approximation is the no-load state, in which some structures may be pre-stretched or residually stressed. The residual strains within the specimen may be approximated by introducing the concept of a "growth tensor" [32].

4. The Finite Element Method for Finite Elasticity

The complex anatomy of the heart greatly influences its mechanical function and little insight is gained by treating it as a simple geometric shape, such as a cylinder or sphere. Consequently, numerical analysis is required to solve the above stress equilibrium equations and the FEM provides the most convenient framework.

4.1. BASIS FUNCTIONS

For FE analysis of finite deformation elasticity problems, it is convenient to choose geometric variables as the dependent variables and interpolate the geometric coordinates (x_1, x_2, x_3) defined at the finite element nodes. Element coordinates (ξ_1, ξ_2, ξ_3) are then normalised material coordinates (see Figure 4), which move with the deforming body and provide the parameterisation of the undeformed and deformed geometric variables:

$$X_i = \Psi_n(\xi_1, \xi_2, \xi_3) X_i^n, \tag{6}$$
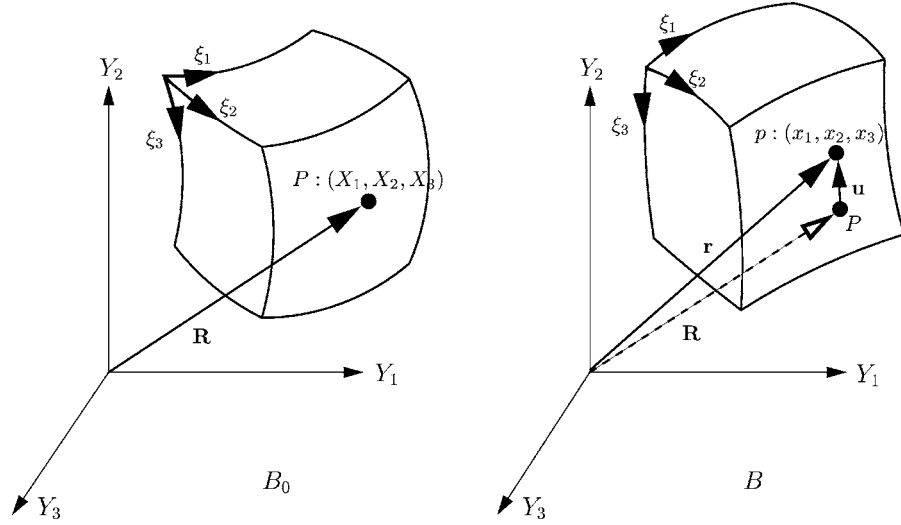$$x_i = \Psi_n(\xi_1, \xi_2, \xi_3) x_i^n, \tag{7}$$

Figure 4. The finite element material coordinate system (ξ_1, ξ_2, ξ_3) is used to identify a material point P in the reference state, which moves through displacement **u** to a new spatial location p in the deformed state.

where $\Psi_n(\xi_1, \xi_2, \xi_3)$ are the chosen 3D basis functions (see below) and X_i^n and x_i^n are the element nodal values (and derivatives) of the ith geometric coordinate in the undeformed and deformed states, respectively.

Since strain (and hence stress) depends on the gradients of these geometric variables, it is convenient to choose cubic Hermite finite element basis functions to ensure derivative continuity across element boundaries. For further information see, for example, [48]. The 1D cubic Hermite interpolation for a field variable u, with nodal parameters u_1 and u_2, and derivatives $(\mathrm{d}u/\mathrm{d}\xi)_1$ and $(\mathrm{d}u/\mathrm{d}\xi)_2$, is given by:

$$u(\xi) = \Psi_1^0(\xi)u_1 + \Psi_1^1(\xi)\left(\frac{\mathrm{d}u}{\mathrm{d}\xi}\right)_1 + \Psi_2^0(\xi)u_2 + \Psi_2^1(\xi)\left(\frac{\mathrm{d}u}{\mathrm{d}\xi}\right)_2, \qquad (8)$$

where the basis functions (shown in Figure 5) are:

$$\begin{aligned}
\Psi_1^0(\xi) &= 1 - 3\xi^2 + 2\xi^3, & \Psi_2^0(\xi) &= \xi^2(3 - 2\xi), \\
\Psi_1^1(\xi) &= \xi(\xi - 1)^2, & \Psi_2^1(\xi) &= \xi^2(\xi - 1).
\end{aligned} \qquad (9)$$

Instead of using the nodal derivative $(\mathrm{d}u/\mathrm{d}\xi)_n$ that depends on the local element ξ-coordinate in the two adjacent elements (which may have different physical lengths), it is more useful to define a global node derivative $(\mathrm{d}u/\mathrm{d}s)_N$, where s is the arc-length and N is the global node number. The ξ-coordinate derivative is then:

$$\left(\frac{\mathrm{d}u}{\mathrm{d}\xi}\right)_n = \left(\frac{\mathrm{d}u}{\mathrm{d}s}\right)_N \left(\frac{\mathrm{d}s}{\mathrm{d}\xi}\right)_n, \qquad (10)$$
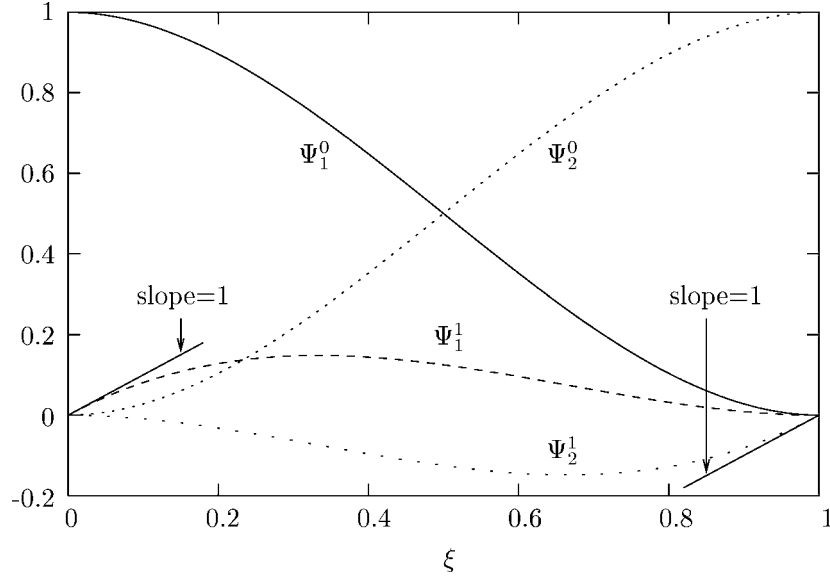
Figure 5. Cubic Hermite basis functions.

where $(\mathrm{d}s/\mathrm{d}\xi)_n$ is an *element scale factor* which scales the arc-length derivative of global node N to the ξ-coordinate derivative of element node n. The result is that $(\mathrm{d}u/\mathrm{d}s)$ is implicitly constrained to be continuous across element boundaries rather than $(\mathrm{d}u/\mathrm{d}\xi)$. The construction of tricubic Hermite basis functions is a straightforward extension of the 1D basis functions and results in 8 parameters per node for each field variable u.

4.2. GALERKIN EQUILIBRIUM EQUATIONS

Using the interpolation functions Ψ_n we can define virtual displacement fields δv_j as:

$$\delta v_j = \Psi_n(\xi_1, \xi_2, \xi_3)\delta v_j^n, \tag{11}$$

where δv_j^n are arbitrary virtual nodal displacements. Substituting equation (11) into the equilibrium equations (equation (4)) and setting the coefficient of each arbitrary displacement component δv_j^n to zero, gives:

$$\int_{V_0} T^{\alpha\beta} F_\beta^j \Psi_{n,\alpha} \, \mathrm{d}V_0$$

$$= \int_{V_0} \rho_0\big(b^j - f^j\big)\Psi_n \, \mathrm{d}V_0 + \int_{S_2} p_{(\mathrm{appl})}\frac{g_{(\xi)}^{3M}}{\sqrt{g_{(\xi)}^{33}}}\frac{\partial x_j}{\partial \xi_M}\Psi_n \, \mathrm{d}S. \tag{12}$$

To evaluate the integrals in equation (12), they must first be transformed from the reference coordinate space to the ξ_M-coordinate space using the appropriate

Jacobian:

$$\iiint_{V_0} T^{\alpha\beta} F^j_{\beta} \Psi_{n,\alpha} \sqrt{G^{(\xi)}} \, d\xi_3 \, d\xi_2 \, d\xi_1 = \iiint_{V_0} \rho_0 (b^j - f^j) \Psi_n \sqrt{G^{(\xi)}} \, d\xi_3 \, d\xi_2 \, d\xi_1$$

$$+ \iint_{S_2} p_{(\text{appl})} g^{3M}_{(\xi)} \frac{\partial x_j}{\partial \xi_M} \Psi_n \sqrt{g^{(\xi)}} \, d\xi_2 \, d\xi_1,$$

(13)

where $\sqrt{G^{(\xi)}} = \sqrt{\det\{G^{(\xi)}_{ij}\}}$ and $\sqrt{g^{(\xi)}} = \sqrt{\det\{g^{(\xi)}_{ij}\}}$ are the Jacobians of the 3D coordinate transformation with respect to the undeformed and deformed configurations, respectively. Note that the surface integral is transformed by substituting $J_{2D} \, d\xi_2 \, d\xi_1$ for dS, where the 2D Jacobian with respect to deformed coordinates is given by $J_{2D} = \sqrt{g^{(\xi)} g^{33}_{(\xi)}}$ [29].

The 3D integrals in equation (13) are evaluated over the undeformed volume and the 2D integral is computed over the portion of the deformed surface (denoted S_2) for which external pressure loads are applied. These integrals are replaced by a sum of integrals over the collection of element domains which constitute the FE model. Element integrals are evaluated numerically using Gaussian quadrature. Components of the second Piola–Kirchhoff stress tensor $T^{\alpha\beta}$ are evaluated at each Gauss point using the constitutive equations below.

4.3. GALERKIN INCOMPRESSIBILITY CONSTRAINT

For incompressible materials, an additional scalar hydrostatic pressure field is introduced into the constitutive equations (see below). The extra constraint necessary to determine the parameters of the hydrostatic pressure field arise from the requirement that the third strain invariant $I_3 = 1$ for incompressible materials.

For a Galerkin formulation, the form of the incompressibility constraints is given by:

$$\iiint_{V_e} (\sqrt{I_3} - 1) \Psi^p \sqrt{G^{(\xi)}} \, d\xi_3 \, d\xi_2 \, d\xi_1 = 0,$$

(14)

where V_e denotes the domain of the element and Ψ^p are the basis functions used to approximate the 3D hydrostatic pressure field. Note that the undeformed 3D Jacobian $\sqrt{G^{(\xi)}}$ is introduced since the integrals are evaluated with respect to the undeformed configuration.

5. Myocardial Material Properties

Heart muscle contains connective tissue and cells, surrounded by fluid-filled extracellular space. Both components consist primarily of water. The nonlinear viscoelastic and poroelastic nature of myocardial tissue has been modelled [14, 44], but this aspect of the material properties is neglected here, where for simplicity we treat the myocardium as an incompressible, elastic solid.

5.1. CONSTITUTIVE RELATIONS

For an incompressible material components of the second Piola–Kirchhoff stress tensor are given by the derivatives of the strain energy function $W(\mathbf{E})$ with respect to the components of $\mathbf{E}$ and a *hydrostatic pressure* (denoted by p), which does not contribute to the deformation, and hence strain energy, of the material [23]:

$$T^{\alpha\beta} = \frac{1}{2}\left(\frac{\partial W}{\partial E_{\alpha\beta}} + \frac{\partial W}{\partial E_{\beta\alpha}}\right) - pa_{(v)}^{\alpha\beta}. \tag{15}$$

The parameters of such a constitutive law can be obtained directly from experiment without reference to the underlying tissue structure. But an approach which incorporates parameters that directly reflect mechanical or structural properties of the material yields a more useful constitutive relation. For example, observed spatial variation in collagen distributions can be related to material constitutive parameters. Section 5.2 details the development of a microstructurally-based constitutive law for passive heart tissue.

Biaxial tension tests on thin sections of ventricular myocardium [6, 10, 33, 46] reveal highly nonlinear, anisotropic stress-strain behaviour (typical of most soft biological tissues). The stress-strain properties along each of the microstructurally relevant directions are quite different, reflecting in part the organisation of collagen relative to these three axes. Figure 6 schematically summarises typical stress-strain behaviour of myocardium when stretched along each of the three microstructural axes [12]. The most striking difference between each of the three axes is the limiting strain for an elastic response. When the tissue is stretched along the fibre direction the limiting extension ratio[*] is about 1.3, whereas the limiting extension
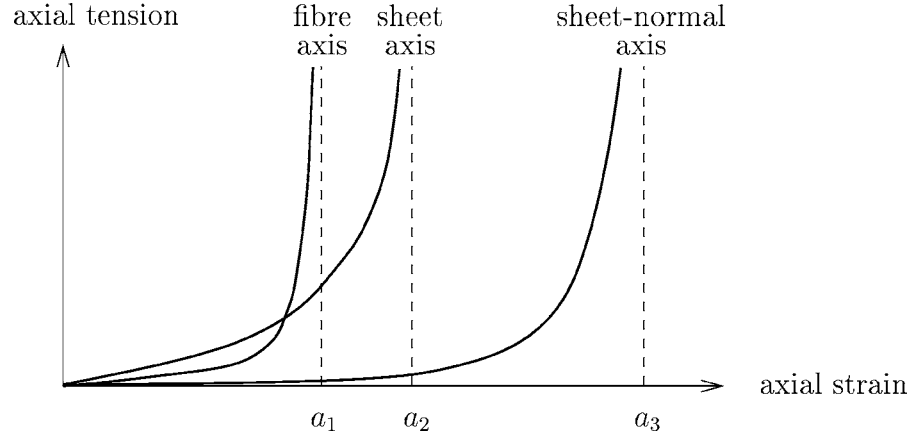

Figure 6. Typical nonlinear stress-strain properties of ventricular myocardium. The parameters a_1, a_2 and a_3 represent the limiting strains for elastic deformations along the fibre, sheet and sheet-normal axes, respectively. Note the highly nonlinear behaviour as the elastic limits are approached.

---

[*] Relative to a resting sarcomere length of approximately 1.95 μm for the unloaded muscle.

ratio for the sheet axis is approximately 1.5. Below an extension ratio of 1.5 very little tension is developed in the direction of the sheet-normal, but tension increases rapidly above this and irreversible damage occurs when this extension ratio exceeds about 1.7 [12].

Variations in the axial limiting strains can be explained by the organisation of the extracellular connective tissue matrix. The high fibre stiffness is most probably due to intracellular titin protein together with the tightly bound endomysial collagen coils that surround individual myocytes [31]. As the tissue is stretched along the fibre axis, these coils straighten and it is the taut length of the collagen that determines the limiting fibre strain [21, 22]. In contrast, the relatively low sheet-normal stiffness is most likely to be due to the sparse array of perimysial collagen links in the cleavage planes between myocardial sheets [19]. Based on this information, a fully 3D orthotropic constitutive law, which incorporates material properties that can be directly estimated from the tissue, is described next.

5.2. THE "POLE–ZERO" CONSTITUTIVE LAW FOR MYOCARDIUM

Stress-strain behaviour along one axis is very nearly independent of the degree of lateral stretch [33]. This means that the contribution to the total strain energy of the stretch along one of the material axes is nearly independent of the contribution from the other two axes – there is, of course, a small degree of cross-axis coupling via the hydrostatic pressure, but this coupling does not occur in a biaxial tension test experiment because the hydrostatic pressure is zero (since the out-of-plane stress is zero). For this reason, the strain energy function is separated into individual expressions in terms of the stretch along each of the material axes. It is also evident from the biaxial tests that the axial stress is very low for small axial strains, but increases rapidly as the strain approaches the limiting strain for that axis. These characteristics, microstructural observations and biaxial test results have been encapsulated in the *pole–zero strain energy function* for myocardium given by:

$$W = k_{11}\frac{E_{11}^2}{|a_{11} - E_{11}|^{b_{11}}} + k_{22}\frac{E_{22}^2}{|a_{22} - E_{22}|^{b_{22}}} + k_{33}\frac{E_{33}^2}{|a_{33} - E_{33}|^{b_{33}}}$$
$$+ k_{12}\frac{E_{12}^2}{|a_{12} - E_{12}|^{b_{12}}} + k_{13}\frac{E_{13}^2}{|a_{13} - E_{13}|^{b_{13}}} + k_{23}\frac{E_{23}^2}{|a_{23} - E_{23}|^{b_{23}}}, \quad (16)$$

where the constitutive parameters (*a*'s, *b*'s and *k*'s) have the following interpretations: The *limiting strains* or *poles*, denoted $a_{\alpha\beta}$, are physical properties of the tissue that may be measured directly from microstructural observations. In particular, [22] used elastica theory on the collagen helices surrounding myofibres to determine the yield strain (pole) of $a_{11} = 0.52$ along the fibre axis. Alternatively, these yield strains can be estimated by fitting the model directly to experimental stress-strain data as is done, for example, by [33]. The second group of parameters, denoted $b_{\alpha\beta}$, are related to the curvature of the uniaxial stress-strain relationships

for each mode of deformation and have been estimated using the biaxial tension test results of [33]. Lastly, the $k_{\alpha\beta}$ parameters weight the contribution of the corresponding mode of deformation to the total strain energy of the material. Estimation of these coefficients is discussed below.

The constitutive parameters of equation (16) are naturally split into six groups, one for each mode of deformation. These groups correspond to the six independent components of Green's strain tensor. The first three terms in equation (16) refer to the three *axial* modes of deformation (fibre, sheet and sheet-normal, denoted 11, 22 and 33, respectively). The parameters associated with these terms have been estimated using a combination of microstructural observations, biaxial tension test results and non-invasive magnetic resonance imaging data, and are listed in Table I. The remaining terms relate to modes of *shear* deformation between the microstructural axes (fibre/sheet, fibre/sheet-normal and sheet/sheet-normal, denoted by subscripts 12, 13 and 23, respectively).

Equation (16) can be regarded as a first order approximation of a power series in the pole–zero terms. A more comprehensive description would include cross-product terms reflecting coupling between different modes of axial and shear deformation and may be warranted following further experimental testing (it cannot be justified on the basis of the biaxial experiments).

It is reasonable to assume that the cellular structures responsible for resisting the shearing deformations are exactly those structures responsible for limiting axial deformations. These load-bearing connections are simply the collagen struts that link individual cardiac fibres and sheets. The important implication of this assumption is that the parameters of the shear terms in equation (16) are strongly correlated to the parameters of the axial terms. The fibre distribution model described below has been used to help understand and quantify some of these parameter correlations.

Table I. Material properties of myocardium for the pole–zero constitutive law.

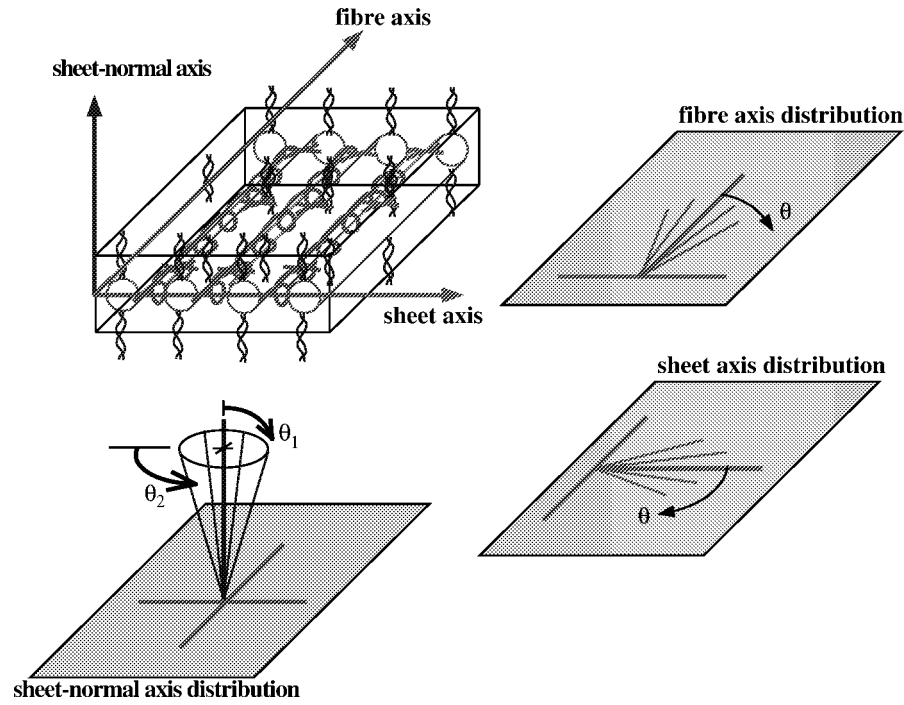| Type	Axial properties		Shear properties	
Coefficients	k_{11}	1.937	k_{12}	1.0
	k_{22}	0.028	k_{13}	1.0
	k_{33}	0.310	k_{23}	1.0
Poles	a_{11}	0.523	a_{12}	0.731
	a_{22}	0.681	a_{13}	0.731
	a_{33}	1.037	a_{23}	0.886
Curvatures	b_{11}	1.351	b_{12}	2.0
	b_{22}	5.991	b_{13}	2.0
	b_{33}	0.398	b_{23}	2.0

Figure 7. The fibre distribution model: orientation of each fibre family about its mean orientation.

Experiments involving shear deformations of cardiac tissue are currently being performed to further validate these correlations [7, 8] and further comments on measuring these shearing characteristics are given in Section 8.

5.3. A FIBRE DISTRIBUTION MODEL FOR CARDIAC TISSUE

A biophysical model of cardiac muscle elasticity is presented here to help understand the correlation between the axial and shear parameters of the pole–zero constitutive law for myocardium [12]. The main assumption of this fibre distribution model is that three families of fibrous connective tissue (mainly collagen) are responsible for storage of the total strain energy of the myocardium. This implies that some axial and shear deformations must be strongly correlated since they involve the same underlying collagen microstructure. The fibre orientations within each family are assumed to be normally distributed about a mean direction, which is aligned with one of the microstructural material axes (see Figure 7). Note that in the following description the term 'fibre' refers to a collagen connection within a fibre family and not a cardiac muscle fibre. The latter will be referred to as a 'myocyte'.

The first fibre family consists of the large coiled perimysial fibres that are closely associated with the myocytes [21, 31]. The mean direction of this family is
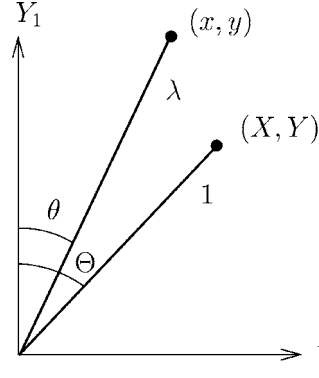
Figure 8. Kinematic analysis of a typical deforming fibre.

coincident with the longitudinal axis of the local myocytes and individual collagen fibres are assumed to lie in the plane of the myocardial sheet. The second family has a mean orientation centred about the sheet axis (which also lies in the sheet plane, but is perpendicular to the myocyte axis) and consists of tightly bound endomysial collagen [2]. The third family of fibres is assumed to have an axisymmetric distribution about a mean direction aligned with the local sheet-normal axis. This family consists of the sparse array of perimysial collagen struts that connect the myocardial sheets.

The variation of connective tissue fibre orientations about their mean directions is assumed to be different for each family of fibres. These variations are defined by standard deviations that describe the distribution of each family of fibres, as illustrated in Figure 7. The first standard deviation defines the variation of the large coiled perimysial collagen fibres about the mean myocyte axis and is therefore relatively small. The second standard deviation defines the variation of the direction of in-sheet endomysial collagen about the local sheet axis and is greater than the first. Two further standard deviations define the axisymmetric variation of the inter-sheet collagen strut direction.

To evaluate the contribution that one particular fibre of a family makes to the total strain energy, consider a unit length fibre in the reference state at an angle of Θ to the Y_1-axis, as illustrated in Figure 8. The Y_1 and Y_2 axes are not material axes (they do not change with material deformation), but rather are local *orthogonal* reference axes with the Y_1 coordinate defined to be aligned with one of the microstructural material axes. In the deformed state, the fibre has length λ and is oriented at an angle of θ to the Y_1-axis. In the undeformed state $X = \cos \Theta$ and $Y = \sin \Theta$, and in the deformed state $x = \lambda \cos \theta$ and $y = \lambda \sin \theta$.

Consider now a particular state of strain in the tissue, characterised by extension ratios λ_1 and λ_2 along the local reference axes Y_1 and Y_2, respectively. These extension ratios can be expressed using:

$$\lambda_1 = \frac{x}{X} = \lambda \frac{\cos \theta}{\cos \Theta}, \qquad \lambda_2 = \frac{y}{Y} = \lambda \frac{\sin \theta}{\sin \Theta}. \tag{17}$$

An expression for the angle of the deformed fibre, θ, is obtained by dividing the extension ratios as follows:

$$\frac{\lambda_2}{\lambda_1} = \frac{\tan \theta}{\tan \Theta} \quad \text{or} \quad \theta = \tan^{-1} \left(\frac{\lambda_2}{\lambda_1} \tan \Theta \right). \tag{18}$$

Thus, given λ_1 and λ_2, a fibre at initial position Θ is rotated to an angle θ and stretched by an extension ratio λ as follows:

$$\lambda = \begin{cases} \lambda_1 \dfrac{\cos \Theta}{\cos \theta}, & \text{when } \theta < \dfrac{\pi}{2}, \\ \lambda_2 \sin \Theta, & \text{when } \theta = \dfrac{\pi}{2}. \end{cases} \tag{19}$$

The fibre strain is calculated from the extension ratio using

$$E_{\mathrm{f}} = \frac{1}{2}(\lambda^2 - 1). \tag{20}$$

The next step is to assume that the fibre orientations for each of the families are normally distributed about their mean directions. In this way, for example, the family of fibres associated with the myocyte axis may be approximated using the Gaussian probability distribution:

$$p_1(\Theta) = \frac{1}{\sqrt{2\pi}\,\sigma_1} \exp\left[-\frac{1}{2} \frac{\Theta^2}{\sigma_1^2} \right], \tag{21}$$

where σ_1 is the standard deviation. Note that the mean of this distribution is aligned with the local myocyte axis in the reference state and that Θ quantifies the *difference* between the direction of a particular fibre and the mean fibre direction.

The total strain energy (due to the deformation) stored in the family of fibres associated with the myocyte axis may be computed by summing up the individual strain energies of all fibres in the family. Equation (22) expresses this sum as the integral over all possible fibres since the probability distribution function varies continuously with the undeformed position Θ. In this expression, k_1, a_1 and b_1 are properties of the family of fibres associated with the myocyte axis. The dependence of the fibre strain E_{f} on Θ is defined using equations (18)–(20)

$$W_1 = \int_{-\pi/2}^{\pi/2} p_1(\Theta) \frac{k_1 E_{\mathrm{f}}^2}{(a_1 - E_{\mathrm{f}})^{b_1}} \, \mathrm{d}\Theta. \tag{22}$$

In a similar manner, the total strain energy stored in the family of fibres associated with the myocardial sheet axis may be calculated using

$$W_2 = \int_{-\pi/2}^{\pi/2} p_2(\Theta) \frac{k_2 E_{\mathrm{s}}^2}{(a_2 - E_{\mathrm{s}})^{b_2}} \, \mathrm{d}\Theta, \tag{23}$$

where $p_2(\Theta)$ is the Gaussian probability distribution function for the family of fibres associated with the sheet axis, k_2, a_2 and b_2 are properties of this family,
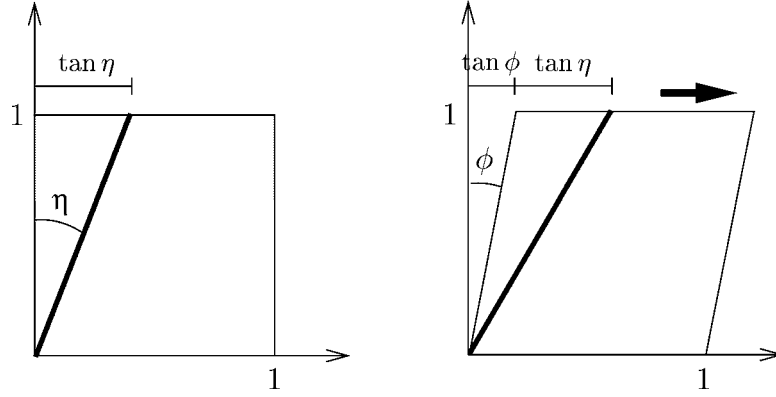
Figure 9. Kinematic analysis of a fibre during simple shear.

and E_s is the material strain along the sheet axis. Note that E_s and $p_2(\Theta)$ may be evaluated using expressions similar to equations (20) and (21), respectively.

The strain energy for the third family of sheet-normal fibres is calculated using equation (24), and the probability distribution function for this family is expressed in equation (25) in terms of the two standard deviations that describe an axisymmetric variation of inter-sheet collagen fibre orientations.

$$W_3 = \int_{\Theta_4=0}^{2\pi} \int_{\Theta_3=0}^{\pi/2} p_3(\Theta_3, \Theta_4) \frac{k_3 E_n^2}{(a_3 - E_n)^{b_3}} \, d\Theta_3 \, d\Theta_4 \tag{24}$$

with

$$p_3(\Theta_3, \Theta_4) = \frac{1}{2\pi \sigma_3 \sigma_4} \exp\left[-\frac{1}{2}\left(\frac{\Theta_3^2}{\sigma_3^2} + \frac{\Theta_4^2}{\sigma_4^2} \right) \right], \tag{25}$$

where E_n is the material strain along the family of collagen fibres associated with the sheet-normal axis and k_3, a_3 and b_3 are properties of this family. Finally, it is assumed that the combined strain energies from each of the three families sum to yield the total strain energy in the tissue.

For present purposes, the fibre distribution model is used to express the limiting strains for shear (namely, a_{12}, a_{13}, and a_{23} in equation (16)) as a function of the axial poles, since it was assumed that the same underlying distributions of collagen connections determine both the tensile and shear characteristics of the tissue. This relationship is derived by considering the kinematics of a typical fibre during a simple shear deformation as shown in Figure 9.

The bold line segment in Figure 9 represents a particular connective tissue fibre oriented at angle η to the mean direction for its family in the reference state. This undeformed fibre has length $\sqrt{1 + \tan^2\eta} = \sec \eta$. During the deformation the fibre moves through a shear angle of ϕ and due to the simple kinematics of the deformation, the deformed fibre length is $\sqrt{1 + (\tan \eta + \tan \phi)^2}$. The extension

ratio (deformed length divided by undeformed length) of the fibre is defined in equation (26) as a function of the undeformed fibre angle η and the shear angle ϕ

$$\lambda_\eta = \sqrt{1 + \tan^2\phi \cos^2\eta + \tan\phi \sin 2\eta}. \tag{26}$$

For a given shear angle ϕ, the fibre angle η^* that produces maximum stretch is found from equation (26) by solving $\partial\lambda_\eta/\partial\eta = 0$ for η^*, resulting in

$$\eta^* = \frac{1}{2}\tan^{-1}(2\cot\phi). \tag{27}$$

As ϕ increases from $0°$ to $90°$, η^* decreases from $45°$ to $0°$. The extension ratio of the fibre with maximum stretch is determined by substituting equation (27) back into equation (26). The maximum extension ratio for a given shear angle is

$$\lambda_{\max} = \frac{1}{2}\left(\kappa + \sqrt{4 + \kappa^2}\right), \tag{28}$$

where $\kappa = \tan\phi$. If this particular fibre yields when its Green's strain reaches the limit $a = \frac{1}{2}(\lambda_{\max}^2 - 1)$, then using some considerable manipulation (see [27]) the maximum possible *elastic* shear strain is

$$\kappa = \frac{2a}{\sqrt{1 + 2a}}. \tag{29}$$

The key point here is that the shear poles of equation (16) (namely, a_{12}, a_{13} and a_{23}) may be directly determined from the limiting strains of the fibre families. For example, consider simple shearing deformations within the plane of the myocardial sheet, referred to here as the $(1, 2)$-plane. The yield strain for a simple shear of the $(1, 2)$-plane in the direction of the myocyte axis (a 2–1 shear) is limited by the *sheet axis pole position* a_{22} since the collagen connections associated with the sheet axis family are put into tension. On the other hand, a 1–2 shear is limited by the *fibre axis pole position* a_{11} since the collagen fibres aligned with the myocyte axis sustain the load. Thus for a general shear of the $(1, 2)$-plane, a reasonable approximation to the limiting shear strain a_{12} may be determined by substituting the minimum of a_{11} and a_{22} into equation (29), which monotonically increases with a. The pole position for the in-plane $(1, 2)$ shear is defined using:

$$a_{12} = \begin{cases} \dfrac{2a_{22}}{\sqrt{1 + 2a_{22}}} & \text{if } a_{22} \leqslant a_{11}, \\[3mm] \dfrac{2a_{11}}{\sqrt{1 + 2a_{11}}} & \text{if } a_{22} > a_{11}. \end{cases} \tag{30}$$

Pole positions for the other shear terms may be determined in an analogous manner.

It remains then to estimate the coefficients and curvature parameters for the shear terms in equation (16). This can be achieved by applying the fibre distribution model to a range of kinematically simple experiments, which involve various axial

and shear deformations. The relative contributions to the strain energy of the tissue can then be used to estimate these unknown parameters (see [27]). Table I lists the material properties used for the modelling in the next section.

6. Passive Inflation during Ventricular Diastole

As an example of applying the constitutive laws discussed above in a finite element model of the intact myocardium, the model is solved here for passive inflation by pressure boundary conditions applied to the left and right ventricular endocardial surfaces of the computational model, illustrated in Figure 10.

Passive ventricular function has been quantified using a variety of global mechanical indices, including the diastolic cavity pressures and volumes, longitudinal elongation, and axial twist of the base relative to the apex. Regional function has been quantified using diastolic strain distributions referred to cardiac wall and fibre coordinate systems (see [38]).

6.1. DIASTOLIC CAVITY PRESSURE AND VOLUME VARIATIONS

The global properties of the diastolic LV have been commonly characterised by the cavity pressure–volume relation. Many studies have quantified this relationship using various techniques in isolated, supported and *in-vivo* hearts. Three canine studies have been selected to assess the accuracy of the pressure–volume relationship predicted by the ventricular mechanics model. For comparison purposes, the ventricular volume has been transformed into a percentage volume change relative to the volume of the unloaded cavity, for which the cavity pressure is zero.
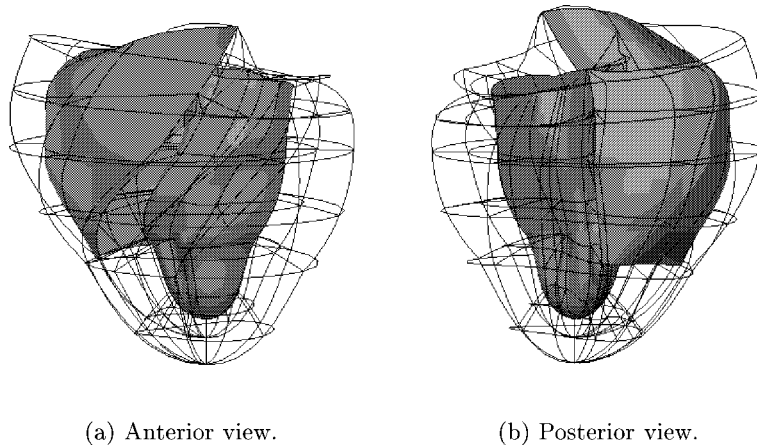

(a) Anterior view.   (b) Posterior view.

Figure 10. Computational model of the cardiac ventricles showing LV and RV endocardial surfaces (shaded) and boundaries of the FE mesh, which consists of 120 tricubic Hermite elements.
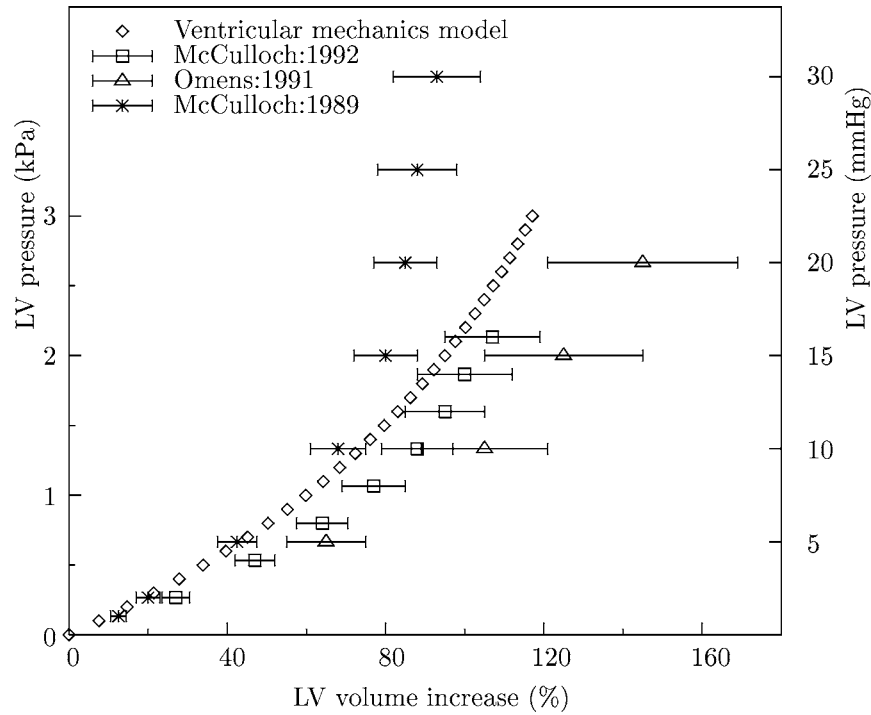
Figure 11. Diastolic pressure–volume relations for the canine LV. The ventricular mechanics model (◊) predicts realistic diastolic stiffening of the LV compared to three experimental studies, all from potassium arrested dog hearts subject to static pressure loading. Error bars show standard deviations.

The ventricular mechanics model was passively inflated to LV and RV pressures of 3.0 kPa (22.5 mmHg) and 0.6 kPa (4.5 mmHg), respectively, using thirty equal load steps. The LV volume was computed at each step, for which the model had converged to an error tolerance of 10^{-3}. Volume changes were normalised by the unloaded LV volume of 32 ml. The predicted normalised passive pressure–volume relationship is represented by diamonds (◊) in Figure 11. It is clear from this comparison that the ventricular mechanics model predicted sufficiently realistic diastolic pressure–volume characteristics.

In seven isolated potassium-arrested canine LVs, [30] quantified 3D principal strains in the equatorial region of the anterior midwall using biplane radiography of three transmural columns of radiopaque beads. Mean strains were reported at four normalised volume changes, which corresponded to approximately 5 ml increments in LV volume. The corresponding LV pressures were estimated from [30] and the authors commented that the angle between the radial axis and the principal axis of greatest thinning (E_3) was <1°. Observations from this study are represented by box symbols (□) in Figure 12.

In comparison, the ventricular mechanics model (◊ in Figure 12) predicts realistic wall thinning (E_3) and minimum in-plane (E_2) strains at the midwall of
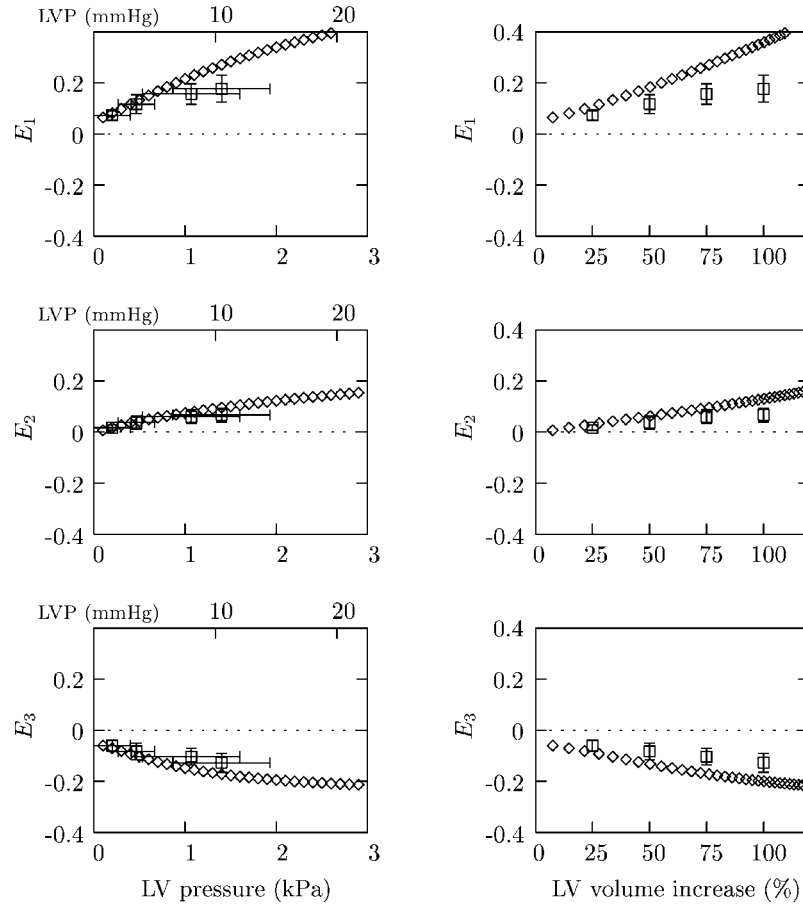
Figure 12. 3D principal strains (E_1, E_2 and E_3) versus LV pressure (LVP) and volume at the midwall of the anterior equatorial region during diastole. Ventricular mechanics model predictions ($\diamond$) are compared to the experimentally observed midwall principal strains (mean $\pm$ SD, $n = 7$) of [30]. See text for explanation.

the anterior LV. However, the predicted maximum principal strain (E_1) illustrates more compliance of the ventricular mechanics model as opposed to the isolated potassium-arrested hearts. More realistic predictions would possibly be achieved if the model had accounted for the heterogeneous material properties of ventricular myocardium.

7. End-Systolic Principal Strains

7.1. ACTIVE CONTRACTION OF MYOCARDIUM

When stimulated, cardiac muscle fibres generate contractile forces. For present purposes, it is assumed that cardiac muscle fibres only generate force in the direction of their longitudinal axes (although models that include active force development

tranverse to the mean fibre axis can lead to more accurate 3D systolic shear strain predictions [38], but this remains to be verified experimentally). This assumption means that just one term must be added to the passive 3D stress tensor of equation (15) to model the active behaviour of myocardium. The additional active stress acts in the muscle fibre direction (aligned with the ν_1-coordinate), and so if the stress tensor is expressed with respect to the microstructural material axes, it is in fact only the T^{11} component that is modified thus:

$$T^{\alpha\beta} = \frac{1}{2}\left(\frac{\partial W}{\partial E_{\alpha\beta}} + \frac{\partial W}{\partial E_{\beta\alpha}}\right) - pa^{\alpha\beta}_{(v)} + Ta^{11}\delta^{\alpha}_1\delta^{\beta}_1, \qquad (31)$$

where $T = T(t, \lambda_{11}, [\text{Ca}^{2+}]_i)$ is the active tension generated by a fibre at time t. For the current modelling, active tension is defined to depend on the time varying muscle fibre extension ratio, $\lambda_{11} = \sqrt{2E_{11} + 1}$, and the concentration of free intracellular calcium, $[\text{Ca}^{2+}]_i$ which is taken to characterise the *level of activation* of a cardiac muscle cell. It is assumed here that the transverse and shear strains have no effect on the active tension generated by the fibres. The steady state mechanical properties of active myocardium are summarised below at a constant level of activation. For more detailed descriptions refer to [11].

The majority of experimental studies that have quantified end-systolic distributions of strain have used the end-diastolic configuration as the reference state. Three such studies have been selected to assess the accuracy of end-systolic principal strain distributions predicted by the ventricular mechanics model. In these studies, E_1 represents maximum shortening and E_3 represents maximum stretch, which is generally associated with wall thickening. ϕ_1 represents the angle to the axis of principal shortening in the plane of the ventricular wall, where positive angles signifies anticlockwise rotations from the circumferential direction.

[42] imaged columns of radiopaque markers implanted in the anterior equatorial LV free wall of seven open-chest dogs. End-systolic 3D principal strains were computed with respect to the end-diastolic reference state. The peak systolic and end-diastolic LV pressures were 16.6 ± 2.5 kPa (125 ± 19 mmHg) and 0.6 ± 0.2 kPa (4.7 ± 1.5 mmHg), respectively. Observations from this study are represented by crosses ($\times$) in Figure 13.

Using similar methods, [39] measured transmural distributions of end-systolic 3D principal strains and directions referred to the end-diastolic state in the anterior equatorial LV free wall of seven open-chest dogs. The peak systolic LV pressure was 16.1 ± 2.9 kPa (121 ± 22 mmHg) and left ventricular end-diastolic pressure (LVEDP) was 0.3 ± 0.2 kPa (2.3 ± 1.5 mmHg). Observations from this study are represented by triangles ($\triangle$) in Figure 13.

[25] analysed the experimental results from a set of bead studies by [41] using non-homogeneous strain analysis. End-systolic 3D principal strains referred to the end-diastolic state were computed for the anterior LV free wall of six open-chest dogs. The peak systolic LV pressure was 15.5 ± 2.8 kPa (116 ± 21 mmHg)
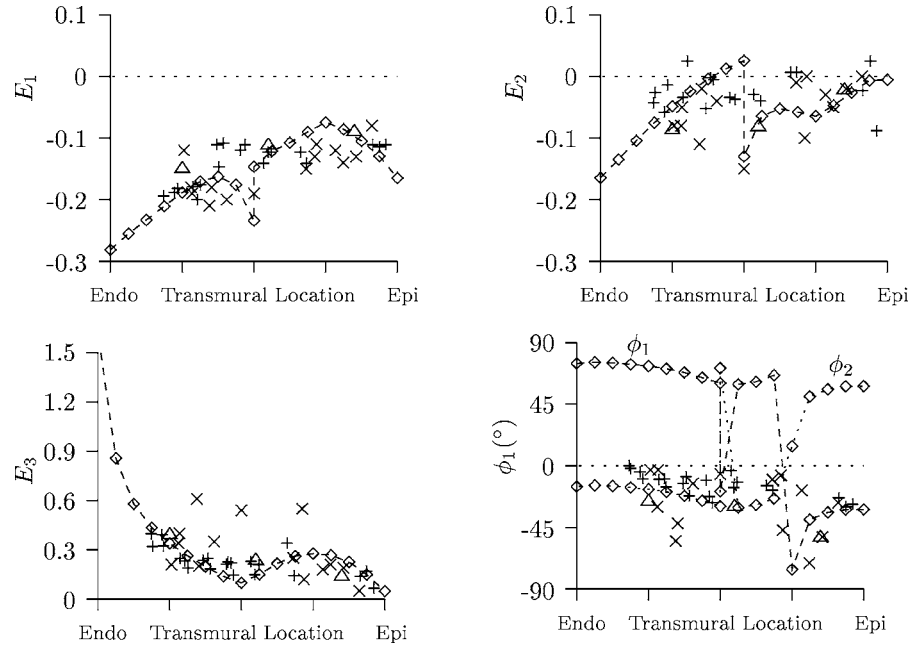
Figure 13. Transmural distributions of 3D principal strain at end-systole (referred to the end-diastolic state) for the equatorial region of the anterior wall. Ventricular mechanics model predictions ($\Diamond$) are compared to experimental observations from [39] ($\triangle$, $n = 7$), [42] ($\times$, $n = 7$) and [41] ($+$, $n = 5$). The predicted in-plane angle to the second principal strain (ϕ_2) is shown for comparison purposes (see text for details).

and LVEDP was 0.7 ± 0.3 kPa (5 ± 2 mmHg). Observations from this study are represented by plus symbols ($+$) in Figure 13.

End-systolic strains for the anterior equatorial LV wall computed using the ventricular mechanics model (represented by diamonds ($\Diamond$) in Figure 13) were referred to the predicted end-diastolic state for comparison with the experimental studies. Reasonable predictions were produced for the maximum shortening (E_1) and thickening (E_3) strains, although the large subendocardial thickening was unrealistic. There are two aspects of myocardial mechanics that are not currently included in the model, which would reduce the unreasonably large subendocardial thickening:

(1) the higher density of collagen fibres in the subendocardium, which would provide a greater constraint on wall thickening; and

(2) the compressibility of the subendocardium due to the movement of blood from subendocardium to subepicardium during systole.

Discontinuities in the distributions of E_1 and E_2 were due to the element interface in the LV midwall and may have revealed a need to either refine the model transmurally or increase the order of the interpolation scheme within the wall plane.

The predicted subepicardial in-plane angle to maximum shortening (ϕ_1) was realistic, but for deeper wall locations there are fundamental differences between

the predicted and reported first principal angles. At approximately 25% of the wall thickness below the epicardium, E_1 and E_2 reach similar magnitudes and there is a marked change in the predicted principal angle ϕ_1 (this is not surprising, since the principal strains and axes are arbitrarily ranked in order of strain magnitude). Interestingly, for the inner three-quarters of the wall the predicted in-plane angle to the second principal strain (ϕ_2) shows reasonable agreement with the reported ϕ_1 measurements. This is not the case at the midwall, however, where the magnitudes of E_1 and E_2 are again very similar and the principal axes seem to switch orientations. For further discussion of the role of the fibre-sheet architecture in myocardial shear deformation and ventricular wall thickening, see [20].

8. Critique of the Ventricular Mechanics Model

In this section we critique the current model and indicate where we believe further developments could improve the model and hence our understanding of ventricular mechanics.

1. *Anatomical model.* The model does not account for myocardial fibres that lie oblique to the ventricular wall surfaces, since the imbrication angle is assumed to be zero at all locations. The computational framework has been developed to incorporate an imbrication angle into the anatomical description, but the ventricular mechanics model awaits further experimental work to characterise the spatial distribution of imbrication angles. This places doubt on model predictions at locations near the apex, where imbrication angles have been reported to descend steeply into the ventricular wall [34]. However, it is unclear at present whether a more realistic representation of the fibre angle distribution in the apical region will greatly influence the global mechanical behaviour of the ventricular myocardium.

2. *Finite element model.* The chosen combination of high order interpolation functions and FE mesh resolution produced sufficiently accurate strain distributions at all locations, except those near the apex. Apical elements of the present ventricular mechanics model must be refined in the longitudinal direction if these locations are of particular interest. Effects of apical mesh refinement have yet to be quantified, but it is unlikely to significantly alter the global ventricular mechanics.

3. *Passive elastic material response.* Several issues must be addressed regarding the passive constitutive law for myocardium (see Section 5.2). The pole–zero law is primarily based on *in-vitro* biaxial tension tests of thin sections of ventricular myocardium. The pole–zero axial weighting coefficients $k_{\alpha\alpha}$, derived from these experiments, may not be appropriate for *in-vivo* mechanics of the ventricles. These constitutive properties may be estimated using *in-vivo* recordings of ventricular deformation and cavity pressures.

    Further research is required to characterise the shear material response of ventricular myocardium. To reconcile the shear response in terms of tissue struc-

ture, Section 5.3 introduced a fibre distribution model for cardiac tissue. Further work is required to interpret shear deformations using this model and to use it to estimate the shear weighting coefficients of the pole–zero law. The shearing behaviour of small cubes of myocardial tissue have recently been measured under various degrees of tissue compression [7, 8] and work is currently underway to fit these results with the pole–zero model and, in particular, to determine whether the nonlinear coupling terms proposed as an extension to the power series in equation (16) are needed.

Finally, the pole–zero law does not provide a suitable description of the compressive response of cardiac tissue. Further experimental studies are required to more accurately model compressive myocardial response.

4. *Regional variation of material properties.* For present purposes, the model incorporated homogeneous material properties throughout the myocardium. Recent microstructural observations suggest that this is an oversimplification of ventricular wall properties. For example, the extent of branching between myocardial sheets changes across the ventricular wall [19]. This implies that the mechanical stiffness along the sheet-normal axis also varies transmurally. In addition, the transmural variation of collagen density has been measured for rat hearts [47], but the appropriate relationship between collagen density and mechanical stiffness remains to be established. Once quantified experimentally, spatially varying material properties could be readily incorporated into the ventricular mechanics model using standard FEM fitting and interpolation techniques. A likely benefit of incorporating stiffer subendocardial tissue properties (resulting from the higher than average density of collagen fibres in this region) may be to reduce the excessive subendocardial wall thickening currently predicted by the model.

5. *3D distributions of residual strain.* The present model accounts for the transmural residual fibre strain distribution, but does not incorporate other components of residual strain. [5] recently quantified 3D distributions of residual strain with respect to the anatomical fibre coordinates. This information could be readily incorporated into the ventricular mechanics model using the growth tensor described by [32].

6. *Myocardial fluid shifts and viscoelasticity.* It is well established that the ventricles stiffen with increased intracoronary blood volume [40]. [13] used an axisymmetric poroelastic model of the LV to illustrate the increase in predicted intramyocardial pressure when redistribution of intracoronary blood was suppressed. Furthermore, [44] used a model that included extracellular fluid flow, which was concluded to account for the insensitivity of experimentally observed passive stress-strain curves to loading rate and of stress-relaxation curves to the amount of stretch. To account for regional myocardial compressibility via changes in vascular volume, we have formulated a simple model of myocardial fluid shift [27]. However, the present study made no provision for the poroelastic or viscoelastic nature of ventricular myocardium, but such con-

siderations would be essential to study the time-varying mechanical response of the ventricles.

7. *Boundary constraints.* A model of the pericardial sac needs to be incorporated into the ventricular mechanics model to restrict filling [36, 37]. Moreover, it is clear that the atria, basal skeleton and chordae tendineae play important roles in restricting the motion of the adjacent portions of ventricular myocardium [35].

8. *Active material response.* For present purposes, a simple steady-state model of the active material response of ventricular myocardium was sufficient to quasi-statically simulate the systolic phase of the heart cycle. To account for the time-varying nature of ventricular activation on heart mechanics, a dynamic model of the active myocardial material response must be incorporated. The computational framework has been formulated to use the time dependent fading memory model for force generation of cardiac muscle fibres [11].

Acknowledgement

References

1. R.J. Atkin and N. Fox, *An Introduction to the Theory of Elasticity*. Longman, London (1980).
2. J.B. Caulfield and T.K. Borg, The collagen network of the heart. *Lab. Invest.* **40**(3) (1979) 364–372.
3. K.D. Costa, P.J. Hunter, J.M. Rogers, J.M. Guccione, L.K. Waldman and A.D. McCulloch, A three-dimensional finite element method for large elastic deformations of ventricular myocardium: Part I – Cylindrical and spherical polar coordinates. *ASME J. Biomech. Engrg.* **118**(4) (1996) 452–463.
4. K.D. Costa, P.J. Hunter, J.M. Rogers, J.M. Guccione, L.K. Waldman and A.D. McCulloch, A three-dimensional finite element method for large elastic deformations of ventricular myocardium: Part II – Prolate spherical coordinates. *ASME J. Biomech. Engrg.* **118**(4) (1996) 464–472.
5. K.D. Costa, K. May-Newman, D. Farr, W.G. O'Dell, A.D. McCulloch and J.H. Omens, Three-dimensional residual strain in midanterior canine left ventricle. *Amer. J. Physiol.* **273** (1997) H1968–H1976.
6. L.L. Demer and F.C.P. Yin, Passive biaxial mechanical properties of isolated canine myocardium. *J. Physiol. London* **339** (1983) 615–630.
7. S. Dokos, B.H. Smaill, A.A. Young and I.J. Le Grice, Anisotropic shear properties of passive ventricular myocardium. *Amer. J. Physiol.* (2001) (submitted).
8. S. Dokos, A.A. Young, B.H. Smaill and I.J. Le Grice, A triaxial-measurement shear-test device for soft biological tissues. *ASME J. Biomech. Engrg.* (2001) (in press).
9. P. Gould, D. Ghista, L. Brombolich and I. Mirsky, *In vivo* stresses in the human left ventricular wall: Analysis accounting for the irregular 3-dimensional geometry and comparison with idealised geometry analyses. *J. Biomech.* **5** (1972) 521–539.
10. J.D. Humphrey, R.K. Strumpf and F.C.P. Yin, Determination of a constitutive relation for passive myocardium: II. Parameter estimation. *ASME J. Biomech. Engrg.* **112** (1990) 340–346.
11. P.J. Hunter, A.D. McCulloch and H.E.D.J. ter Keurs, Modelling the mechanical properties of cardiac muscle. *Prog. Biophys. Molec. Biol.* **69** (1998) 289–331.

12. P.J. Hunter, M.P. Nash and G.B. Sands, Computational electromechanics of the heart. In: A.V. Panfilov and A.V. Holden (eds), *Computational Biology of the Heart*. Wiley, West Sussex, England (1997) Chapter 12, pp. 345–407.

13. J.M. Huyghe, T. Arts, D.H. van Campen and R.S. Reneman, Porous medium finite element model of the beating left ventricle. *Amer. J. Physiol.* **262** (Heart Circ. Physiol. 31) (1992) H1256–H1267.

14. J.M. Huyghe, D.H. van Campen, T. Arts and R.M. Heethaar, A two-phase finite element model of the diastolic left ventricle. *J. Biomech.* **24**(7) (1991) 527–538.

15. R.F. Janz and A.F. Grimm, Finite-element model for the mechanical behaviour of the left ventricle: Prediction of deformation in the potassium-arrested rat heart. *Circ. Res.* **30** (1972) 244–252.

16. R.F. Janz and A.F. Grimm, Deformation of the diastolic left ventricle. I. Nonlinear elastic effects. *Biophys. J.* **13** (1973) 689–704.

17. A.M. Katz, *Physiology of the Heart*, 2nd ed. Raven Press, New York (1992).

18. P. Kohl, P. Hunter and D. Noble, Stretch-induced changes in heart rate and rhythm: Clinical observations, experiments and mathematical models. *Prog. Biophys. Molec. Biol.* **71**(1) (1999) 91–138.

19. I.J. Le Grice, B.H. Smaill, L.Z. Chai, S.G. Edgar, J.B. Gavin and P.J. Hunter, Laminar structure of the heart: Ventricular myocyte arrangement and connective tissue architecture in the dog. *Amer. J. Physiol.* **269**(38) (1995) H571–H582.

20. I.J. Le Grice, Y. Takayama and J.W. Covell, Transverse shear along myocardial cleavage planes provides a mechanism for normal systolic wall thickening. *Circ. Res.* **77** (1995) 182–193.

21. D.A. MacKenna, J.H. Omens and J.W. Covell, Left ventricular perimysial collagen fibers uncoil rather than stretch during diastolic filling. *Basic Res. Cardiol.* **91**(2) (1996) 111–122.

22. D.A. MacKenna, J.H. Omens, A.D. McCulloch and J.W. Covell, Contributions of collagen matrix to passive left ventricular mechanics in isolated rat hearts. *Amer. J. Physiol.* **266** (1994) H1007–H1018.

23. L.E. Malvern, *Introduction to the Mechanics of a Continuous Medium*. Prentice-Hall, Englewood Cliffs, NJ (1969).

24. A.D. McCulloch, Cardiac biomechanics. In: J.D. Bronzino (ed.), *The Biomedical Engineering Handbook*. CRC Press, Boca Raton, FL (1995) Chapter 31, pp. 418–439.

25. A.D. McCulloch and J.H. Omens, Non-homogeneous analysis of three-dimensional transmural finite deformation in canine ventricular myocardium. *J. Biomech.* **24**(7) (1991) 539–548.

26. I. Mirsky, Ventricular and arterial wall stresses based on large deformation analyses. *Biophys. J.* **13**(11) (1973) 1141–1159.

27. M.P. Nash, Mechanics and material properties of the heart using an anatomically accurate mathematical model. PhD Thesis, The University of Auckland, New Zealand (1998).

28. P.M.F. Nielsen, I.J. Le Grice, B.H. Smaill and P.J. Hunter, Mathematical model of geometry and fibrous structure of the heart. *Amer. J. Physiol.* **260** (Heart Circ. Physiol. 29) (1991) H1365–H1378.

29. J.T. Oden, *Finite Elements of Nonlinear Continua*. McGraw-Hill, New York (1972).

30. J.H. Omens, K.D. May and A.D. McCulloch, Transmural distribution of three-dimensional strain in the isolated arrested canine left ventricle. *Am. J. Physiol.* **261** (Heart Circ. Physiol. 30) (1991) H918–H928.

31. T.F. Robinson, M.A. Geraci, E.H. Sonnenblick and S.M. Factor, Coiled perimysial fibers of papillary muscle in rat heart: Morphology, distribution and changes in configuration. *Circ. Res.* **63** (1988) 577–592.

32. E.K. Rodriguez, A. Hoger and A.D. McCulloch, Stress-dependent finite growth in soft elastic tissues. *J. Biomech.* **27**(4) (1994) 455–467.

33. B.H. Smaill and P.J. Hunter, Structure and function of the diastolic heart: Material properties of passive myocardium. In: L. Glass, P.J. Hunter and A.D. McCulloch (eds), *Theory of Heart:*

Biomechanics, Biophysics, and Nonlinear Dynamics of Cardiac Function. Springer, New York (1991) pp. 1–29.

34. D.D. Streeter, Jr., H.M. Spotnitz, D.P. Patel, J. Ross, Jr. and E.H. Sonnenblick, Fibre orientation in the canine left ventricle during diastole and systole. *Circ. Res.* **24** (1969) 339–347.

35. Y. Takayama, I.J. Le Grice, J.W. Holmes and J.W. Covell, Effects of chordal uncoupling on deformation in the papillary muscle. *FASEB J.* **8**(5) (1994) A591.

36. J.V. Tyberg and E.R. Smith, Ventricular diastole and the role of the pericardium. *Herz* **15**(6) (1990) 354–361.

37. G.S. Tyson, Jr., G.W. Maier, C.O. Olsen, J.W. Davis and J.S. Rankin, Pericardial influences on ventricular filling in the conscious dog: An analysis based on pericardial pressure. *Circ. Res.* **54** (1984) 173–184.

38. T.P. Usyk, R. Mazhari and A.D. McCulloch, Effect of laminar orthotropic myofiber architecture on regional stress and strain in the canine left ventricle. *J. Elasticity* **61** (2000) 143–164.

39. F.J. Villarreal, W.Y.W. Lew, L.K. Waldman and J.W. Covell, Transmural myocardial deformation in the ischemic canine left ventricle. *Circ. Res.* **68**(2) (1991) 368–381.

40. W.M. Vogel, C.S. Apstein, L.L. Briggs, W.H. Gaasch and J. Ahn, Acute alterations in left ventricular diastolic chamber stiffness: Role of the erectile effect of coronary arterial pressure and flow in normal and damaged hearts. *Circ. Res.* **51**(4) (1982) 465–478.

41. L.K. Waldman, Y.C. Fung and J.W. Covell, Transmural myocardial deformation in the canine left ventricle: Normal *in vivo* three-dimensional finite strains. *Circ. Res.* **57**(1) (1985) 152–163.

42. L.K. Waldman, D. Nossan, F. Villareal and J.W. Covell, Relation between transmural deformation and local myofiber direction in the canine left ventricle. *Circ. Res.* **63** (1988) 550–562.

43. R.H. Woods, A few applications of a physical theorem to membranes in the human body in a state of tension. *J. Anat. Physiol.* **26** (1892) 362–370.

44. M. Yang and L.A. Taber, The possible role of poroelasticity in the apparent viscoelastic behaviour of passive cardiac muscle. *J. Biomech.* **24**(7) (1991) 587–597.

45. F.C.P. Yin, Ventricular wall stress. *Circ. Res.* **49**(4) (1981) 829–842.

46. F.C.P. Yin, R.K. Strumpf, P.H. Chew and S.L. Zeger, Quantification of the mechanical properties of noncontracting canine myocardium under simultaneous biaxial loading. *J. Biomech.* **20** (1987) 577–589.

47. A.A. Young, I.J. Le Grice, M.A. Young and B.H. Smaill, Extended confocal microscopy of myocardial laminae and collagen network. *J. Microsc.* **192**(2) (1998) 139–150.

48. O.C. Zienkiewicz and R.L. Taylor, *The Finite Element Method. I. Basic Formulation and Linear Problems*, 4th ed. McGraw-Hill, Berkshire, UK (1994).